Article

Experimental Study of a Gurney Flap on a Pitching Wind Turbine Airfoil under Turbulent Flow Conditions

Junwei Yang [1,2], **Hua Yang [1,*]**, **Xiangjun Wang [1]** and **Nailu Li [1]**

1   College of Electrical, Energy and Power Engineering, Yangzhou University, Yangzhou 225127, China; yangjunwei@yzu.edu.cn (J.Y.); x.j.wang@yzu.edu.cn (X.W.); nlli@yzu.edu.cn (N.L.)
2   Guangling College, Yangzhou University, Yangzhou 225000, China
*   Correspondence: yanghua@yzu.edu.cn; Tel.: +86-138-1583-8009

Abstract: The present work aimed to investigate the aerodynamic characteristics of a pitching wind turbine airfoil with a Gurney flap under turbulent inflow. Experiments were carried out for the DTU-LN221 offshore wind turbine airfoil under different turbulence levels at Reynolds number 10^5 order of magnitude by replacing the grilles in the wind tunnel. The dynamic stall characteristics were analyzed by measuring surface pressure and near-wake flow field. The pressure results demonstrated that with the increase of turbulence intensity, the differences in lift hysteresis loops between baseline airfoil and flapped airfoil became smaller. With the turbulence intensity from 0.5% to 10.18%, the maximum lift increment of the Gurney flap decreased from 14.32% to 4.34% (i.e., 0–20° pitching oscillation). In a more extensive range of oscillation, the capability for the lift-improvement dropped down a bit more (i.e., 0–25°). A brief aerodynamic damping analysis indicated that the Gurney flap was more stable in turbulent conditions than the baseline airfoil. Besides, hysteresis loops of the wake were analyzed to compare the difference between the flapped airfoil and the baseline airfoil. Unlike the studies of static airfoils, the results may help better understand the dynamic characteristics of offshore wind turbines with Gurney flaps for practical situations.

Keywords: wind tunnel experiment; aerodynamic characteristics; gurney flap; dynamic stall; turbulent inflow

1. Introduction

In the face of the Paris agreement being finalized, all contracting countries need to contribute to dealing with global climate change. Developing wind energy technology has become an international consensus, making the wind energy industry own relatively mature technology and commercial development systems. Further improving the utilization rate of wind turbines is an inevitable topic in wind energy development. Therefore, the Gurney flap has attracted many researchers' attention as a simple structure with higher energy efficiency. After the pioneering work of Liebeck [1], several seminal types of research have led to a deep understanding of the features of the Gurney flap, including the influence of the geometrical shape, Reynolds number (Re) and attached position. Furthermore, optimal operating conditions were obtained when the height of the Gurney flap was between 1% and 3% [2–5]. It is widely believed that the vortices separated from the suction and pressure sides have different intensities, so the flow of the counter-rotating asymmetric vortex in the near wake effectively increases the radian of the airfoil. According to the Kutta conditions, the flow always intersects in the baseline airfoil cases at the trailing edge. In contrast, in the flapped airfoil cases, the flow is diverted to a point away from the airfoil surface, increasing lift ability [6], and the drag increase is slight when the Gurney flap height is less than the boundary layer thickness [7]. Kentfield [8,9] conducted wind tunnel tests on a small-scale wind turbine with a Re of 6×10^4 and field tests on a 65 kW full-size wind turbine with Gurney flaps. The measurement results proved the efficiency of Gurney flaps, with the power of the full-size wind turbine increasing by 4.3% in a

month. Another example was the DTU-10 MW wind turbine designed by Bak et al. [10]. The method of improving aerodynamic performance was put forward by adding Gurney flaps with a chord length height of 1% to 3%, and the designed results were verified by software EllipSys3D finally. Ebrahimi and Movahhedi [11] numerically investigated the flow behavior and the output power caused by the Gurney flap based on the NREL Phase VI wind turbine. Results confirmed that the shaft power could be increased by up to 17% at most. Yan et al. [12] obtained similar results from vertical axis wind turbines at a low tip speed ratio. Alber et al. [13] experimentally investigated the rotating effect of the Gurney flap on a model wind turbine. The results showed that the Gurney flaps provide better axial wake velocity and lift coefficient performance. Recently, Gurney flaps have attracted industry attention. The Vestas® (global largest wind power manufacturer) optimization service, for example, claims that Gurney flaps increase the annual energy production of a wind turbine by 1.2% per year [14].

However, there exist many challenges in accurately understanding and predicting unsteady blade aerodynamic loads and rotor performance, among which the dynamic stall is the most important [15]. The occurrence of dynamic stall is related to the sharp increase of the unsteady flow. In the actual operation of wind turbines, turbulent incoming flow, gust, yaw bias and blade torsion all cause local changes in the angle of attack (AOA) of each airfoil section. If the degree of change is sufficient, then the boundary layer on the blade surface cannot immediately follow the change of the AOA. As a result, a dynamic stall occurs. The dynamic stall characteristics can be well reflected by the airfoil motion through the pitch oscillation [16,17]. For measuring the unsteady dynamic stall flow field, Mulleners and Raffel [18] combined time-resolved particle imaging and surface pressure analysis to explain the stall flow development. The experimental results verified that the dynamic stall behavior is highly correlated with flow separation and reattachment. The dynamic stall development can be divided into the primary instability stage of the initial development of the shear layer and then the vortex formation stage of the large-scale vortex formed by the shear layer rolling up. On that basis, Gupta and Ansell [19] performed a detailed time-frequency analysis using pressure measurements. The results indicated that during the dynamic stall process, the main characteristic of the flow around the airfoil is the reverse flow of boundary layer separation from the leading and trailing edges.

Rival and Tropea [20] conducted dynamic stall experiments on the SD7003 airfoil with different oscillation forms. They concluded that airfoils' aerodynamic force and vortical wake changed significantly with the reduced frequency. Masdari et al. [21] experimentally studied the lift characteristics of a pitching wind airfoil in the light stall and deep stall regions, using the normal force defect (NFD) to characterize the hysteresis loop of lift at $Re = 4.2 \times 10^5$. The conclusions demonstrated that lift characteristics had a strong correlation between the mean AOA (α_{mean}) and the amplitude of pitch motion (A). The increase in amplitude delayed the AOA at which the maximum lift was located. The pressure measurement of a supercritical airfoil with a series of combined motions was reported by Tabrizian et al. [22] when the Re was 8.76×10^5. Consequently, the instantaneous pressure was obtained at the flow separation, reattachment and vortex formation states. Mamouri et al. [23] analyzed various parameters affecting the aerodynamic coefficient of the dynamic stall by using two load cells, including reduced frequency, α_{mean}, pitching amplitude and Re. Subsequently, the experimental airfoil was optimized to make it more suitable for the dynamic stall condition. The authors suggested selecting a more suitable airfoil according to the rotation frequency of the wind turbine.

Some researchers also had examined the dynamic stall characteristics combined with the Gurney flaps. Gerontakos and Lee [24] experimentally studied the dynamic stall characteristics of NACA 0012 airfoil with 1.6% and 3.2% chord-height Gurney flaps when the Re was 1.07×10^5. The results presented that the dynamic stall angle can be changed by controlling the mounting angle of the Gurney flaps. Masdari et al. [25] investigated the influence of the Gurney flap's height and mounting angle on the pitching NACA 0012 airfoil numerically. The study results mentioned that increasing the reduced frequency

and oscillation amplitude could improve the maximum lift coefficient and the lift curve slope. Zanotti and Gibertini [26] tested the aerodynamic characteristics of Gurney flaps with active form installed on pitching airfoils in a wind tunnel. The research stated that the lift coefficients of the airfoil could be increased in the upstroke motion, and the Gurney flap retracted in the downstroke motion to reduce the possibility of stall flutter.

Many recent studies, as mentioned above, have used experimental measurements, flow visualizations and numerical simulations to study the dynamic stall. The aerodynamic characteristics of the oscillating airfoil were evaluated by comparing various parameters, such as the impact of α_{mean}, reduced frequency, Re and the amplitude, which vividly demonstrated the evolution of the dynamic stall vortex, boundary layer and the hysteresis loop. Considering the natural wind turbines operating in a highly turbulent region, conclusions about the Gurney flap drawn from uniform inflow may not be accurate. For similar research, Li et al. [27] evaluated the influence of turbulent inflow coupled with pitching motion on the performance of a wind turbine airfoil. The results demonstrated that a turbulent boundary layer was formed near the leading edge, narrowing the range of the hysteresis loop with the increase of turbulence intensity (T.I.). At last, the authors proposed doing more studies on turbulent inflow to guide for improving the efficiency of wind turbines.

To sum up, both the dynamic stall phenomenon and the Gurney flaps have remarkable effects on aerodynamic loads. Therefore, the research in this paper focuses on the unsteady aerodynamic characteristics of the flapped airfoil under various turbulence intensities. Surface pressure and near wake flow distribution were obtained using an electronic pressure acquisition system and the hot-wire anemometry. The aim was to reveal the dynamic stall characteristics of a flapped airfoil in turbulent conditions by experiments. Quantitative information includes: (1) instantaneous pressure coefficients, (2) lift hysteresis loops, (3) wake hysteresis loops. Besides, other valuable information investigated from this experiment, such as the flow separations and aerodynamic damping analysis, was presented in the current paper. Finally, the conclusion was accompanied by a discussion of the experimental investigations.

2. Experimental Methodology

2.1. Experimental Setup

All experiments were performed in the low speed, closed-circuit wind tunnel test area of Yangzhou University (China), with a contraction ratio of 9:1. The test section was a rectangular shaped space with the cross-section parameters of 0.4 m · 0.4 m, and the length was 1.0 m. A 2.5 kW power fan drove the stream, with the frequency converter can precisely adjust the velocity from 1.5 to 40 m/s. The difference was less than 1% of the average value of the test section with the turbulence level was less than 0.5% based on measurements with a hot-wire probe (type 55P61).

The schematic diagram and photo of the experimental setup are shown in Figure 1. For the present study, the DTU-LN221 airfoil model was adopted [28], which has a chord length of 0.15 m with a span length of 0.395 m. The Technical University of Denmark designed this offshore wind turbine airfoil type with low noise, low sensitivity to roughness, high lift, and lift to drag ratio at middle range Reynolds numbers. An aerodynamic test validated the designed airfoil in the wind tunnel of LM Wind Power [29]. In our experiment, the tested airfoil and Gurney flap were all manufactured by 3D printing technology, and the flap was designed as a rectangle section with a height of 1.5% chord length and thicknesses of 0.75% chord length.

Moreover, the airfoil was assembled from three sections, where 61 small taps were averagely arranged on the middle section with a diameter of 0.0011 m. Thus, a more accurate pressure description can be obtained. The airfoil model was placed vertically in the test section and connected to a servo motor (80AEA07530-SC3) via a rotating shaft with a diameter of 0.01 m at a quarter chord length. Therefore, instantaneous AOA can be controlled by a programmable motion controller, with the minimum instruction unit

being 0.0001 m. These taps were connected by a digital pressure acquisition system (DTC Initium) via hollow plastic hoses on the model's backside. The measuring range of the equipment was ±2.5 kPa with an accuracy of 0.05% and 333.3 Hz sampling frequency. Besides, a multi-axis force balance (Gamma SI-65-5) was placed below the servo motor to verify the correctness of the pressure measurement. Finally, a motorized moving frame and a hot-wire anemometer (CTA/HWA) were employed to describe the wake flow of the airfoil.
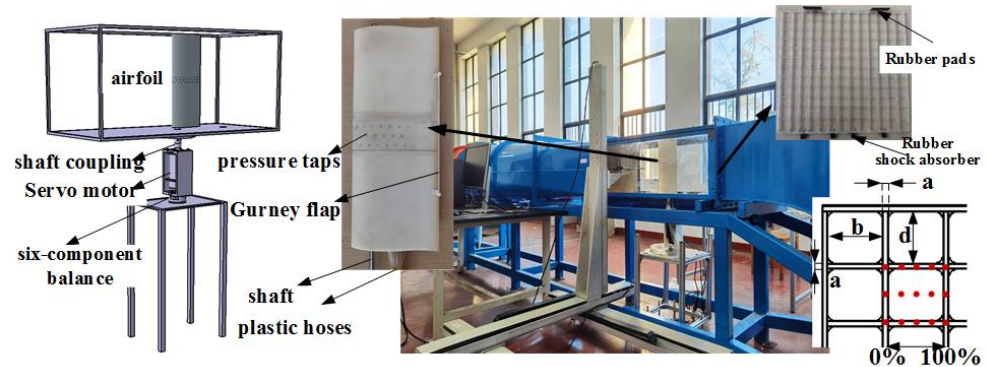
Figure 1. 3 D model of the test setup and pitching oscillation mechanism used in the test.

As demonstrated in the top right of Figure 1, grilles used in this test were assembled by acrylic strip and connected with adhesive. Rubber shock absorbers were put on the bottom of the grilles. Rubber pads were also added between the top and the wind tunnel wall to increase the friction force. In this figure, a, b and d represent the width of the grilles the horizontal and vertical spacing of the grilles, respectively. The red dots in this figure exhibit the measured positions in a mesh through a hot-wire probe (type 55P61). The sampling frequency was 5 kHz, and the grilles were placed at the test section entrance. For better comparison, two distinct types of grilles were used, and the geometric dimensions were given in Table 1. The distance between the grilles and the leading edge of the airfoil was 0.42 m. According to Vita et al. [30], in a grille-generated flow field, the turbulent flow was fully developed when $D/M \geq 5$ and isotropic when $D/M \geq 10$, where D represents the distance between the grilles and the measuring point, M represents the mesh size. In this experiment, M was approximately defined as $(b + d)/2$. Therefore, the values of D/M in the two cases were about 16.37 and 10.66, respectively, to meet the isotropy requirement.

Table 1. Dimensions of grilles.

	a (m)	b (m)	d (m)
Scheme 1	0.005	0.0253	0.026
Scheme 2	0.008	0.0408	0.038

2.2. Data Processing Methodology

Figure 2 shows the schematic diagram of the tested airfoil, where red spots in the figure represent real pressure taps arranged on the airfoil section. Therefore, aerodynamic performances can be obtained through the pressure measurement described subsequently.

For dynamic stall research, the lift hysteresis loop was one of the most critical aerodynamic parameters to get stall information. It could be achieved by integrating the instantaneous pressure coefficient along the airfoil surface, and then the instantaneous pressure coefficient C_{pi} was introduced as Equation (1).
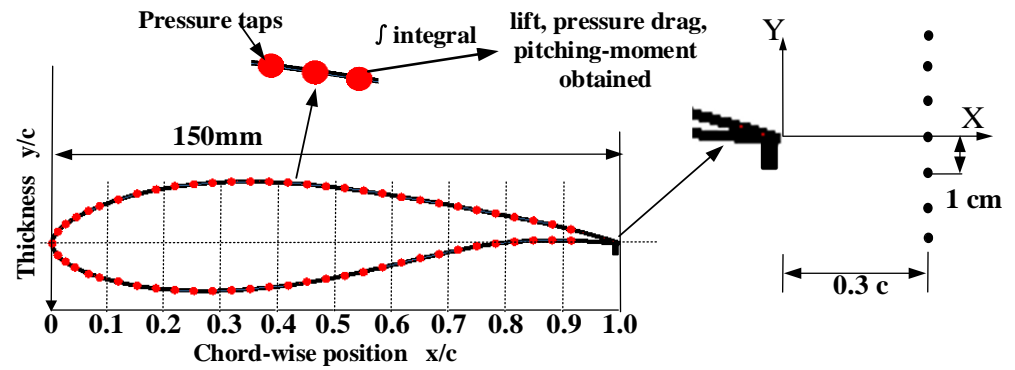
Figure 2. Schematic diagram of the DTU-LN221 airfoil used in the experiment.

$$C_{pi} = (p_i - p_0)/(0.5\rho U_0^2), \tag{1}$$

where p_i is the instantaneous pressure tested by pressure tap of i (i = 1 to 61), p_0 is the average static pressure tested by two pitot tubes placed on the side forward position of the airfoil, ρ is the air density, and U_0 is the velocity of inflow.

Therefore, the hysteresis curves of lift and pitching moment coefficients were obtained by combining the instantaneous pressure with the contact position. Equations (2) and (3) gave instantaneous lift coefficient C_l and pitching moment coefficient C_m.

$$C_l = C_n \cos \alpha - C_t \sin \alpha \tag{2}$$

$$C_m = \int_0^1 \left(C_{pl} - C_{pu} \right)(0.25 - \hat{x})d\hat{x}, \tag{3}$$

where

$$C_n = \int_0^1 (C_{pl} - C_{pu})d\hat{x} \tag{4}$$

$$C_t = \int_{\hat{y}_{l\,max}}^{\hat{y}_{u\,max}} (C_{p,be} - C_{p,af})d\hat{y}, \tag{5}$$

where α represents the angle of attack; $\hat{x}$ is the value of relative chord length; $\hat{y}$ is the value relative thickness length; C_n and C_t represent the normal and tangential force coefficient, respectively; C_{pu} and C_{pl} are the pressure coefficients on the suction and pressure sides of the airfoil, respectively; $C_{p,be}$ and $C_{p,af}$ represent the pressure coefficient before and after the max thickness of the airfoil; $\hat{y}_{u\,max}$ and $\hat{y}_{l\,max}$ represent the relative max thickness values on both the suction and pressure sides.

In order to illustrate the Gurney flap efficiency better, the pressure drag C_{d_p} was also calculated, which was expressed as follows.

$$C_{d\_P} = C_n \sin \alpha + C_t \cos \alpha. \tag{6}$$

The effect of blockage in the wind tunnel experiment is inevitable. We believe that due to the blockage, the cross-sectional area in the wind tunnel will decrease, increasing the inflow velocity. Hence, the aerodynamic forces may tend to be larger. In this dynamic airfoil experiment, the maximum blockages were 9.8% and 15.8% in wake and pressure measurements, respectively. The values were close to the previous airfoil aerodynamic studies such as 13.7% (AOA = 26°, Masdari et al. [21]), 12% (AOA = 40°, Choudhry et al. [31]), 14.0% (AOA = 25°, Granlund et al. [32]), 10.3% (AOA = 20°, Li et al. [33]), 9% (AOA = 15°, Masdari et al. [34]). Considering these data were analyzed in an uncorrected manner or not mentioned of the correction. Moreover, no reliable and general methods could modify blockage for dynamic cases [35]. Consequently, the data were analyzed directly in this experiment. To solve this question, we need to carry out a series of wind-tunnel experiments to make it clear in the next research.

The dynamic experimental conditions need to be determined in this experiment, and the instantaneous AOA was defined in Equation (7).

$$\alpha = \alpha_{\text{mean}} + A\sin(2Kt), \qquad (7)$$

where K is reduced frequency, it is a dimensionless quantity that reveals the instability of the flow around an airfoil, which is introduced as follows, $K = \omega c/2U_0$, c is the chord length and ω is the airfoil angular velocity. When $K = 0$, the flow is in a stable state; when $K \geq 0.005$, the flow is in an unstable condition. Due to the motor limitation, severe vibration would occur when the K value was too large. To ensure that the number of samples in each pressure measurement cycle was enough [22]. Hence, the fixed value of reduced frequency was chosen ($K = 0.0167$, providing about 626 samples per cycle).

In addition, as shown in Figure 2, a coordinate system was established at the airfoil's trailing edge (when $\alpha = 0°$). The X and Y axes were set in the horizontal and vertical directions, respectively. The schematic spots arranged on the right of the coordinate axis represented the hot-wire anemometer measuring positions set downstream of the trailing edge. The sampling rate was also set at 5 kHz.

Uncertainty analysis of the pressure measurements in the present study was considered by using the standard deviation as the error bars, which consisted of suggestions from similar experiments [26,27]. By this method, the uncertainties can be solved by a large number of samples and multiple measurements for the Gurney flap [36]. For the hot-wire anemometer and angle settings, wake velocities were accurate acquired due to the high precision of a data acquisition device and a servo-controlled motor. Note that the accuracies of the hot-wire anemometer and servo motor reach 0.001 V and 0.2%, respectively. Therefore, we thought that the uncertainty for velocities in wake measurements was relatively negligible.

3. Results and Discussion

The dynamic stall could be classified into the attached flow, light stall and deep stall when the airfoil section was undergoing different AOAs. In order to cover all these ranges, these values of parameters were represented in Table 2. For a better comparison, the following results were presented at a fixed inflow velocity of 15 m/s corresponding to Re about 1.5×10^5. In addition, to display the wake variation before and after stall and compare turbulent inflow effects, the wake hysteresis loops were measured in a small pitching motion range of 8.8°–15.2° using a hot-wire anemometer.

Table 2. Pressure measurement plan.

A (°)	α_{mean} (°)	K	Test Grilles
10	10	0.0167	none, Scheme 1, 2
12.5	12.5	0.0167	none, Scheme 1, 2

3.1. Turbulence Test Results

Firstly, the T.I. of the flow field calibration of the grilles was carried out. The T.I. results at different positions of a mesh are shown in Figure 3a, turbulence dissipated behind the grilles, and eventually, the flow tended to be stable. The values of T.I. in two test meshes were steady. The T.I. in scheme 2 was higher than scheme 1, though the blocking effect of the two grilles was similar (approximately 70%) while scheme 2 used the thicker grilles. In two schemes, the average T.I. corresponding to the airfoil's leading edge were 6.35% and 10.18%, respectively.
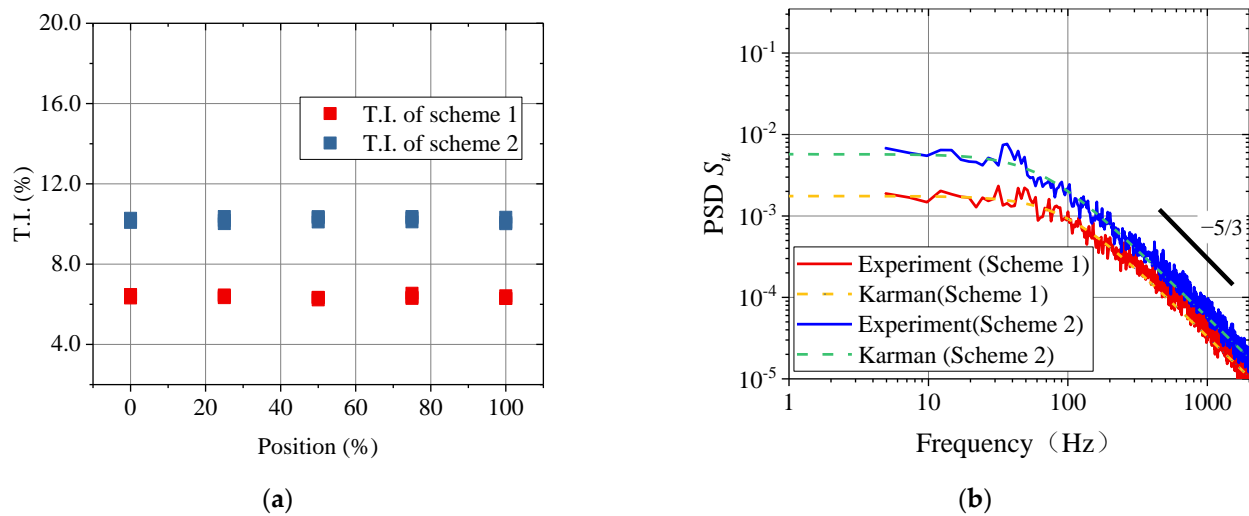
Figure 3. Description of turbulent flow parameters. (**a**) T.I. description at the position of leading edge; (**b**) power spectral density (PSD).

It should be noted that the integral length scale was another parameter of turbulent flow statistics. However, this was ignored in many airfoil aerodynamic analyses [37]. Although the integral scale was generally small in a wind tunnel test using passive grilles. In this study, the integral scales of the two gratings were about 0.013 m and 0.015 m, respectively. Therefore, the study in this paper was based on similar integral scales and different turbulence intensities. Figure 3b shows the PSD at the central measuring position. The Welch technique and a rectangular window were used to estimate the spectra, the number of Discrete Fourier Transform was 2048 with 50% segment overlap, and the frequency step was 2.44 Hz. The spectral values of the two schemes were consistent with the corresponding Karman spectra with a good agreement for the $-5/3$ law. By comparison, it is found that the PSD of the frequency of the vortices that mainly generate energy was below 40 Hz. Similar structural grilles inevitably made the distribution of turbulent energy in the frequency domain have a certain similarity.

3.2. Experiment Validation

In order to verify the accuracy of the results, the DTU-LN221 airfoil was analyzed aerodynamically under uniform inflow. The lift coefficients were chosen as a validation case with error bars representing the standard deviation. Figure 4a compares the lift coefficients of the integral pressure method and balance measurement. The Xfoil software package was also used to compute lift coefficients of the baseline airfoil. According to the pressure test, static lift coefficients pulsated after the stall due to the shedding vortex and flow separation. Under static conditions, the baseline airfoil attained a maximum lift coefficient of 1.428 with a stall angle of about 12°, while the flapped airfoil reached 1.600. The experimental data were acceptable with the data produced by Xfoil before the stall, and the stall angle was nearly the same. (The T.I. was set at about 0.3% in Xfoil, the transition position was set at 20% of the suction surface relative to the chord length).

In order to further illustrate the possible validity of the conclusions in this paper on a full-size wind turbine, it was necessary to be concerned about the Reynolds effect. Based on similar research [37], Figure 4b exhibited the lift coefficient results measured in uniform flow conditions [29,38] to reflect the possible relation. It can be found that when the Re was 1.5×10^5, there was an approximate relationship between the lift coefficients with a higher Re, so the Reynolds effect was not evident in this experiment.
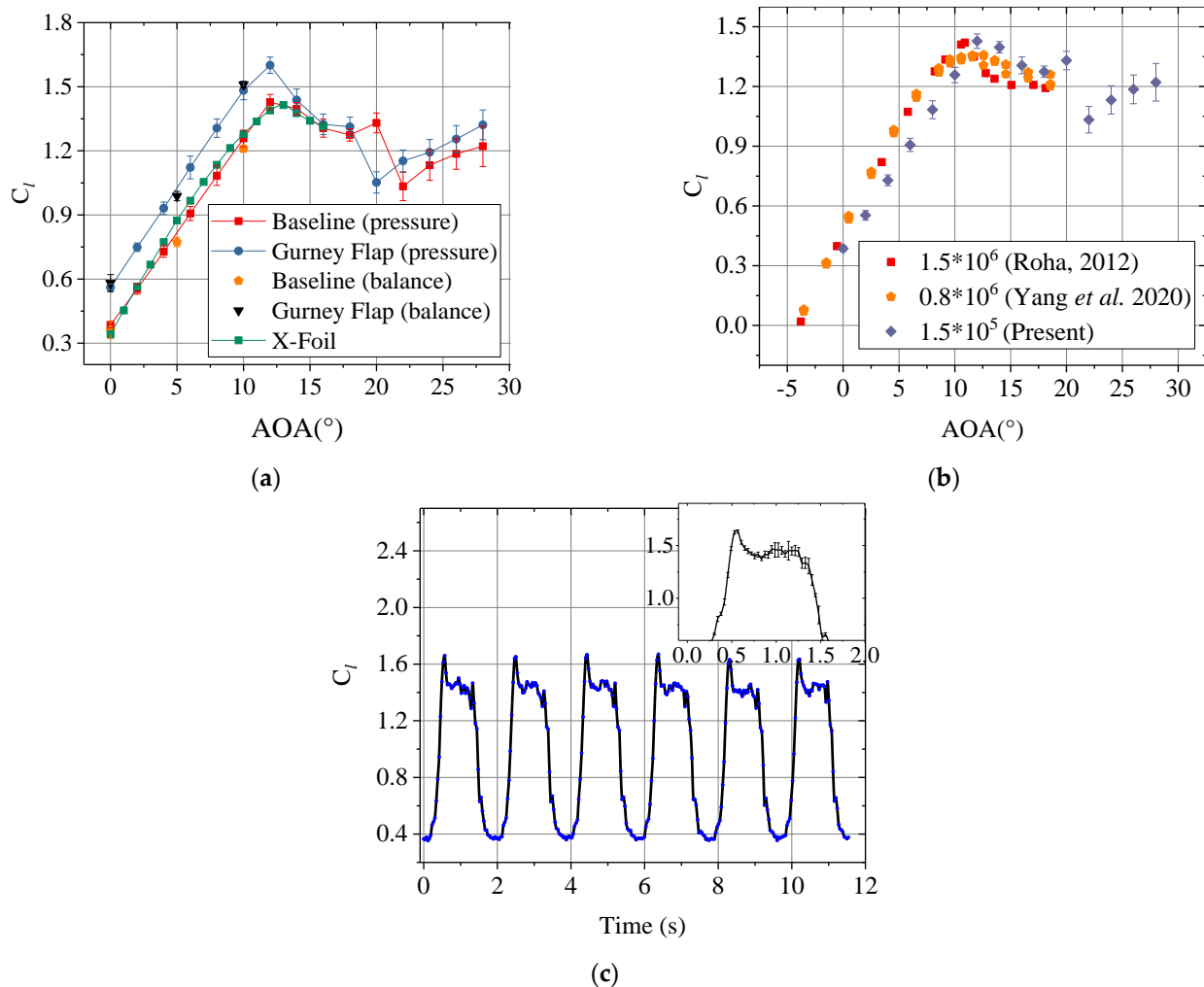
Figure 4. Validation of the aerodynamic results of DTU-LN221 airfoil. (**a**) Static state (**b**) Reynolds effect (**c**) Dynamic state.

For the repeatability evaluation of the dynamic results, Figure 4c demonstrates the time history of the dynamic lift coefficients for $A = 10$, $\alpha_{mean} = 10$ and $K = 0.0167$. Acceptable repeatability of the phase averaged values of lift coefficients were observed. The fluctuations near the stall region of downstroke motion, as shown in the right top with phase averaged values, and standard deviations were caused by the randomness of large vortical structures [26]. Hence, measurements were performed several times, and the subsequent analyses of the measured data were all averaged.

### 3.3. Surface Pressure Characteristics

In this section, the results of pressure distribution were discussed. The effects of the turbulent inflow and Gurney flap on the pitch oscillation were also analyzed. Figure 5 demonstrates the evolution of the dynamic pressure distributions in a pitching cycle, seen from Figure 5a, in the prior-stall condition (period < 25%), the airfoil was characterized by reverse flow and expanded to the upstream, then formed a slight leading edge vortex (LEV) and developed to the downstream. With the increase of the AOA, the LEV gradually appeared and began to grow due to the accumulation of reverse flow at the trailing edge and the leading edge shear layer away from the airfoil surface. The giant vortex formed has a peak value on the suction surface during the period ≈ 0.3. Since then, the airfoil experienced a light stall, but owing to the delay of boundary layer flows, even after the maximum AOA (period ≥ 50%), there was still a near-peak value on the suction surface within the downstroke motion range. Along with the downstroke motion, the strength of
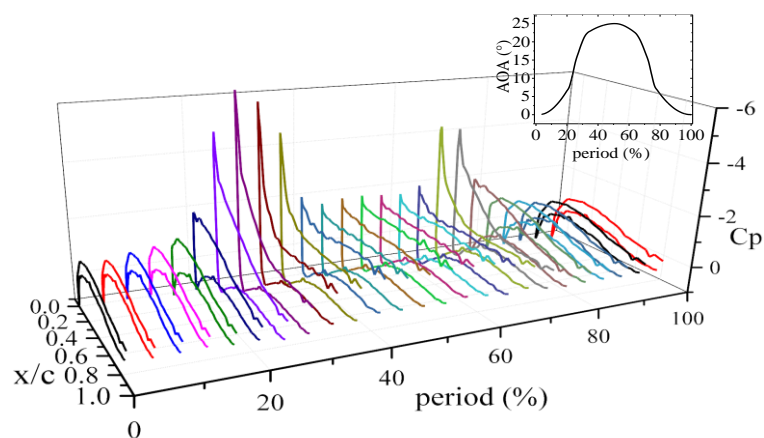
the LEV decreased, the suction peak shrunk on the suction surface and disappeared at the period $\approx 70\%$.
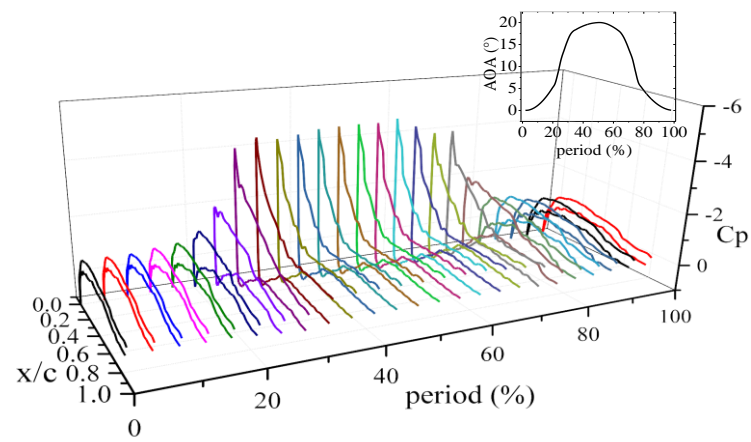

(**a**)
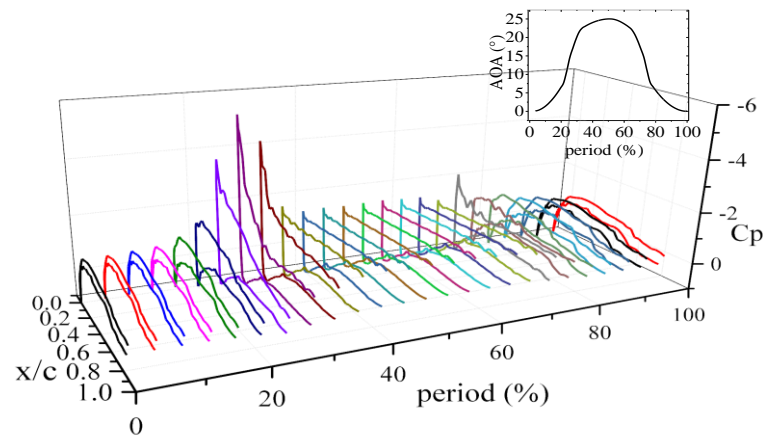
(**b**)

(**c**)

Figure 5. Comparison of the Cp distributions in an oscillatory period. (**a**) uniform inflow, $A = 10$, $\alpha_{\text{mean}} = 10$; (**b**) uniform inflow, $A = 12.5$, $\alpha_{\text{mean}} = 12.5$; (**c**) T.I. of 10.18%, $A = 12.5$, $\alpha_{\text{mean}} = 12.5$.

For the case of a deep stall, as shown in Figure 5b, the airfoil experienced a deep stall delay, and finally, the flow was completely attached. After the period >30%, the

pressure suddenly dropped, and the LEV overflowed on the suction surface. At this step, the flow produced by the dynamic stall vortex was completely separated. The pressure of the suction surface became flat, and the surface pressure of the airfoil changed little at the beginning of the downstroke. The situation was markedly different from the static stall condition. The static stall separation first occurred at the airfoil's trailing edge and propagated upstream, eventually causing the complete separation in the suction surface. Until the beginning of the flow reattachment (period ≈ 80%), the pressure coefficients were gradually increased. In addition, compared with the uniform flow, pressure coefficients in the turbulent situations were changed obviously in the stall zones, especially on the suction surface. As shown in Figure 5c, with the increase of the T.I., the peak value at the leading edge of the suction surface was more prominent, and the range was broader. The presence of turbulence made the airfoil enter a deep stall and reattachment state at a greater AOA in one cycle.

The next step in this study will investigate the dynamic characteristics of the Gurney flap. Figure 6 shows the dynamic and static pressure distributions of the baseline airfoil and flapped airfoil around 4°, 12° and 18° under uniform inflow. The lift-improvement interpretation of Gurney flaps can be revealed by showing the instantaneous pressure at different positions during a pitching cycle. The horizontal axes show the chord-wise positions, and the vertical axes represent the pressure coefficients. Meanwhile, the lift coefficients of dynamic and static states under three kinds of turbulent inflow are exhibited in Figure 7. The translucent areas represent the standard deviations of multiple measurements.
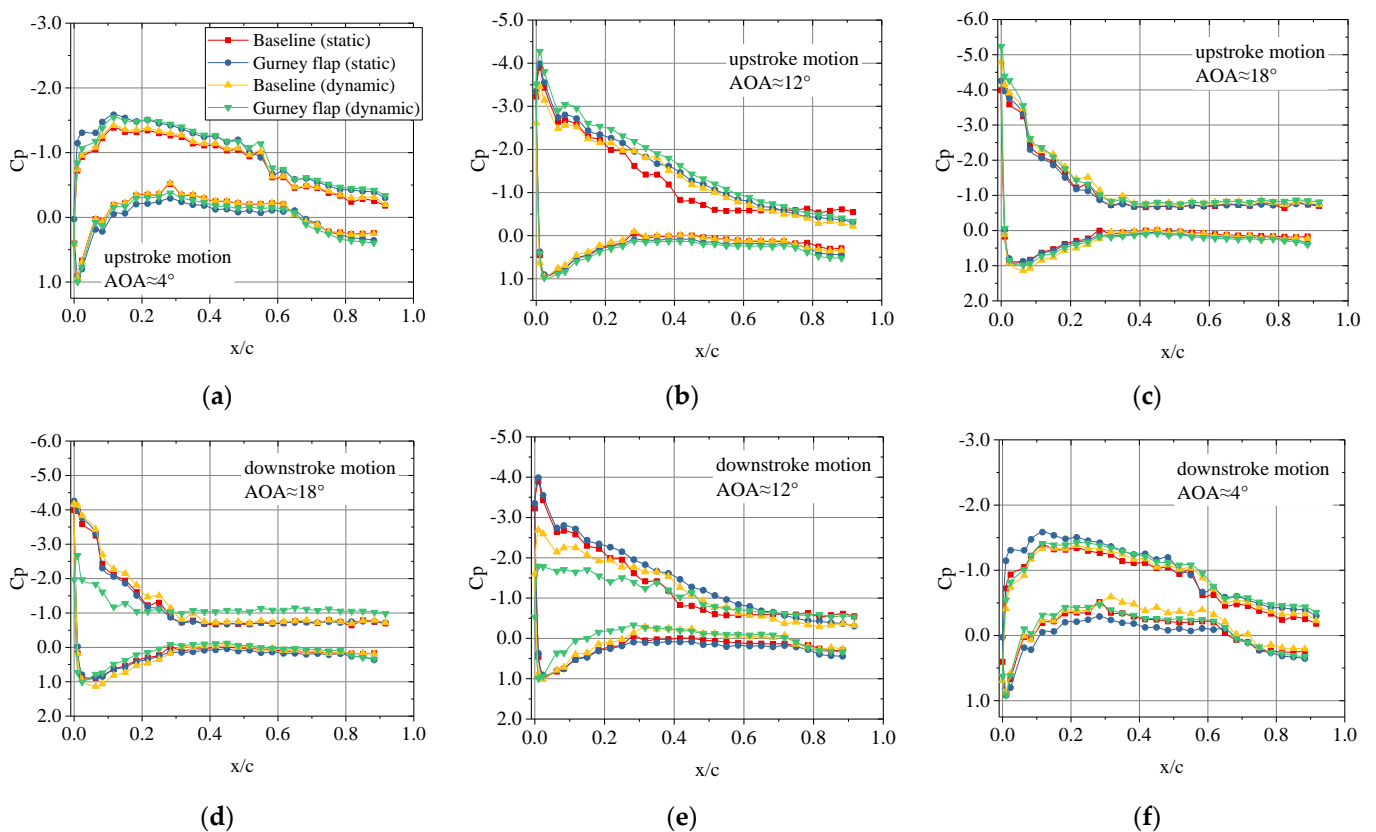
Figure 6. Comparison of the pressure coefficient measured for $A = 10$, $\alpha_{\mathrm{mean}} = 10$ and $K = 0.0167$ in a period at the uniform inflow. (**a**) upstroke, AOA ≈ 4°; (**b**) upstroke, AOA ≈ 12°; (**c**) upstroke, AOA ≈ 18°; (**d**) downstroke, AOA ≈ 18°; (**e**) downstroke, AOA ≈ 12°; (**f**) downstroke, AOA ≈ 4°.
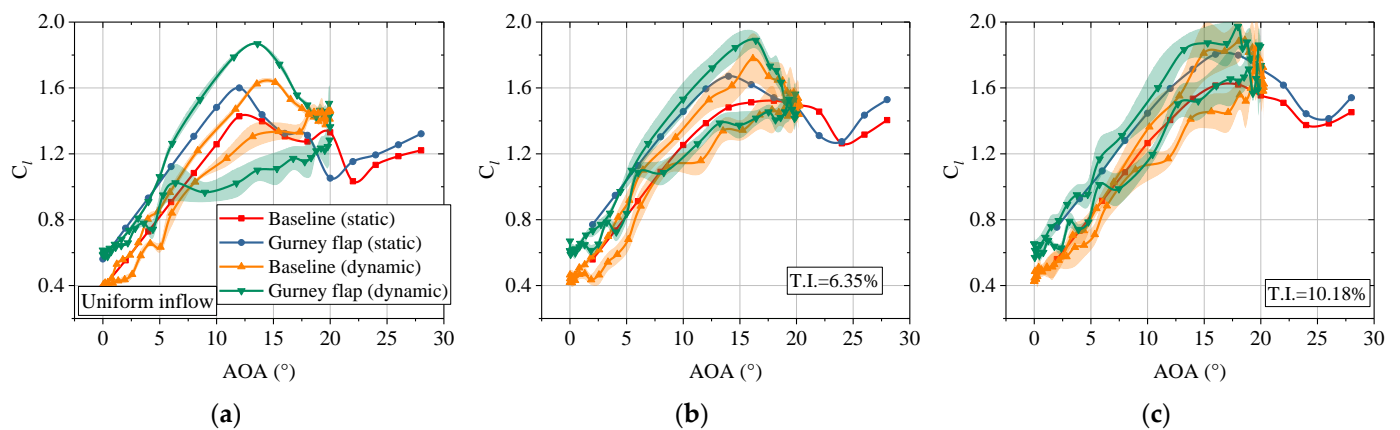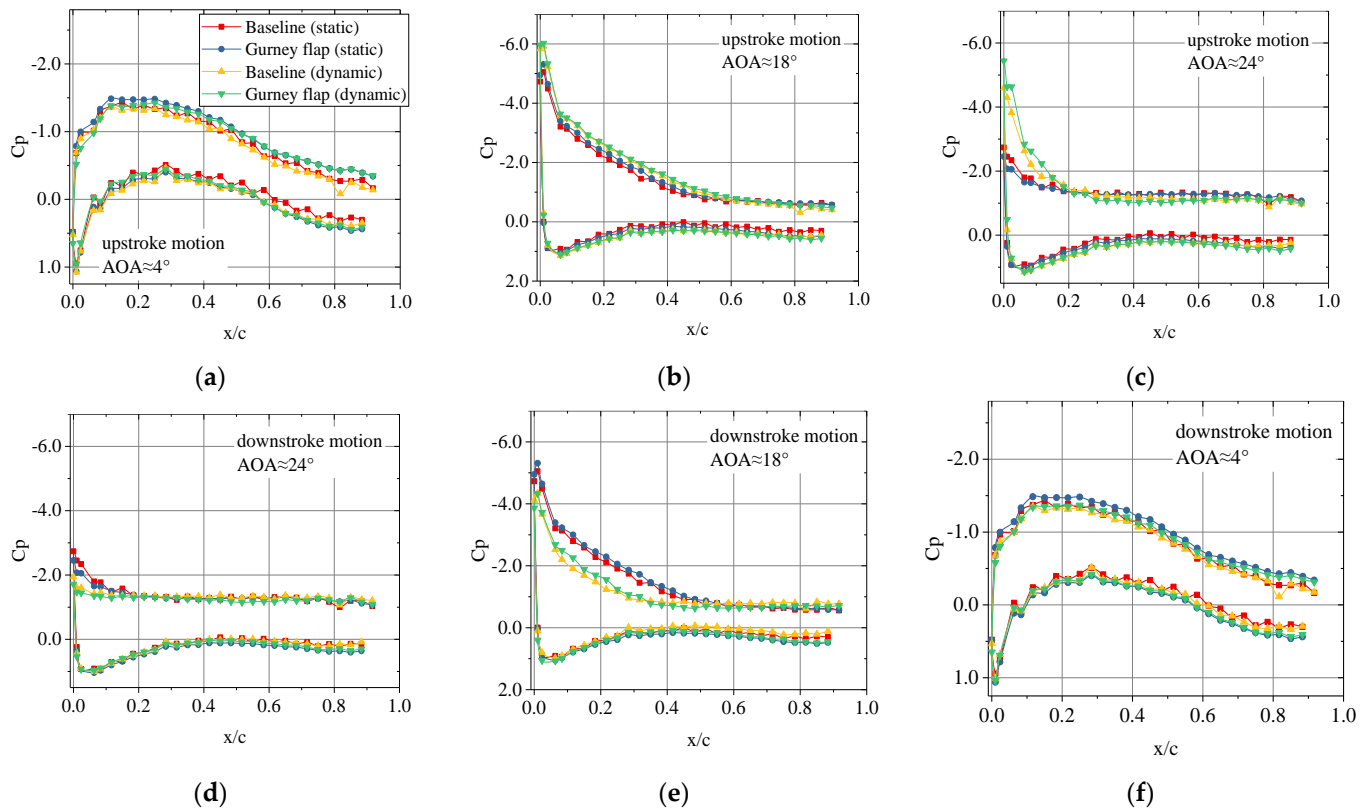
Figure 7. Comparison of lift coefficients for $A = 10$, $\alpha_{\mathrm{mean}} = 10$ and $K = 0.0167$. (**a**) uniform inflow; (**b**) T.I. of 6.35%; (**c**) T.I. of 10.18%.

As can be seen from Figure 6a,b, the increase in lift caused by the Gurney flap resulted from the combined action of more significant pressure on the upper and lower surfaces of the airfoil. With the increase of AOA, Figure 6b shows the situation of 12° in upstroke motion. At this moment, the pressure of static baseline airfoil on the suction surface tends to be flattened. While the flow was still attached to the surface in dynamic conditions, this was due to the transient variation of the leading stall vortex and the so-called effects of boundary layer improvement [23,24]. The suction surface has more momentum to resist the adverse pressure gradient in dynamic conditions, enabling the boundary layer to withstand greater flow separation than static conditions. However, with the AOA increasing continually, as seen in Figure 7a, the lift of the baseline airfoil dropped rapidly after it reached the peak of 1.634 (AOA = 15.16°), in contrast with the flapped airfoil arrive in 1.869 at 13.60°. This situation was attributed to the dynamic lift stall caused by the overflow of LEV. Installing a Gurney flap in a dynamic state of uniform inflow could make the flow separation point move forward. In Figure 6c, the flow was completely separated behind 30% of the suction surface in all cases. While in downstroke motion (see Figure 6d,e), the flow of the flapped airfoil showed a more obvious delay than that of the baseline airfoil, which produced a locally lower negative pressure on the leading edge of the suction surface. This situation can also serve as illustrated by the enormous hysteresis curve of the flapped airfoil in Figure 7a. With the flap install, the hysteresis loop became more expansive in the uniform case, and the lifting capacity increased from static 12.04% to dynamic 14.32%.

Besides, the lift coefficients of turbulent conditions were compared in Figure 7b,c. As the T.I. increased, the hysteresis loops were smaller than the uniform inflow case for the flapped airfoil. Under the three dynamic conditions, the maximum lift of the flapped cases was increased by 14.32%, 6.24% and 4.34%, when the T.I. were 0.5%, 6.35% and 10.18%, respectively. Indicating that the maximum lift between the two airfoil cases became smaller with the T.I. increased. Due to the high turbulence, the boundary layer can withstand excessive adverse pressure gradient, and the flow could reattach to the airfoil surface in the range of large AOAs. Then the circulation around the airfoil increases consistently. In terms of the Kutta–Joukowskis theorem, the lift increases accordingly. At this time, the lift and the circulation of the baseline airfoil have significantly increased relative to the uniform condition and may approach a limit value. Therefore, it might reduce lift efficiency by reducing the part of a Gurney flap that increases the lift.

The performance of the airfoil with a fluctuation width of 12.5°, acquired under turbulent inflow conditions, was also presented in Figure 8 for comparison. As seen from Figure 8a,f, the situations were similar to light stall cases during the attached flow. The decrease in the suction peak at AOA ≈ 24° (see Figure 8c) indicated that the airfoil had stalled during the upstroke motion. Moreover, the airfoil exhibited a more evident stall phenomenon during the downstroke motion (see Figure 8d). At this time, the pressure

integral areas of the dynamic conditions were smaller than those under static conditions. Compared with the light stall zone, the baseline airfoil and flapped airfoil became relatively flat on the suction surface. As seen in Figure 8e, both two dynamic cases entered the reattachment process, and the separation point of the flapped airfoil was closer to the trailing edge than that of the baseline airfoil, although the change was small.
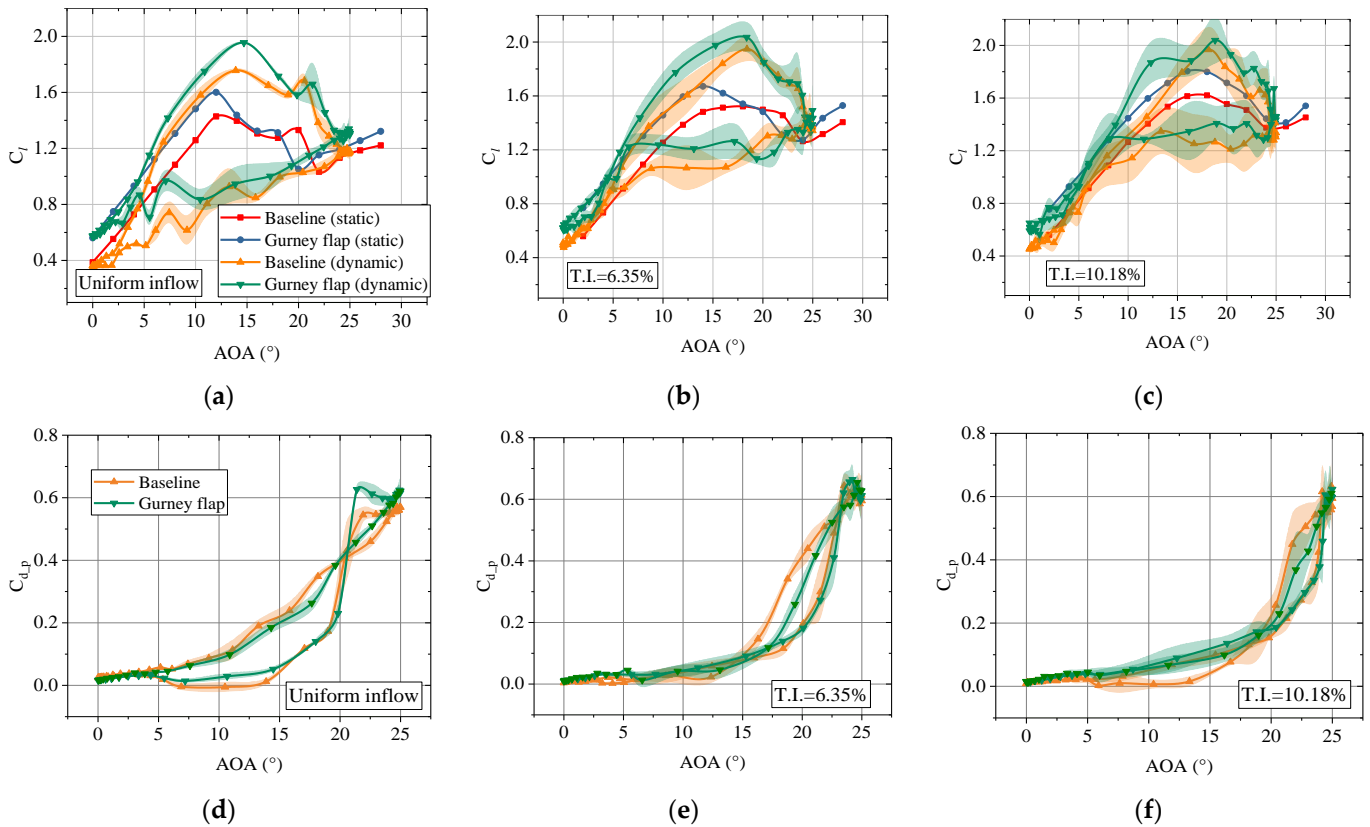

Figure 8. Comparison of the pressure coefficient measured for $A = 12.5$, $\alpha_{mean} = 12.5$ and $K = 0.0167$ in a period at T.I. of 10.18%. (**a**) upstroke, AOA $\approx 4°$; (**b**) upstroke, AOA $\approx 18°$; (**c**) upstroke, AOA $\approx 24°$; (**d**) downstroke, AOA $\approx 24°$; (**e**) downstroke, AOA $\approx 18°$; (**f**) downstroke, AOA $\approx 4°$.

Figure 9 shows the lift hysteresis loops in the deep stall region under three turbulent inflow conditions. Contrasted from Figure 7, the hysteresis loops were all enlarged with the increase of pitching amplitude. Moreover, under different turbulent inflow, the lift overshoots near 20° in upstroke motion were caused by the flow fluctuation in the unstable stall state. When the values of T.I. were 0.5%, 6.35% and 10.18%, the maximum lift of the flapped airfoil were increased by 11.33%, 4.47% and 3.61%, respectively. Compared to the baseline airfoil, the higher T.I. could markedly reduce the maximum lift capacity of a Gurney flap. However, in all tested conditions, lift coefficients of the Gurney flap were higher than those of the baseline airfoil most of the period, and these increases were all evident.

In the experiment, acquiring total drag was arduous because the pressure measurement could not obtain the viscous drag at a small AOA. Hence, pressure drags of the airfoil were compared, total drag can be considered dominated by pressure drag at large AOAs. Results can be observed in Figure 9d–f that the Gurney flap had smaller drags at large AOAs in turbulent conditions. So, we can at least reasonably speculate that installing the Gurney flap at a large AOA was meaningful. This conclusion was consistent with our previous static experiment that the Gurney flap has better aerodynamic performance at a moderate T.I. inflow condition [38].

Figure 9. Comparison of lift and pressure drag coefficients *A* = 12.5, α_{mean} = 12.5 and *K* = 0.0167. (**a**) lift coefficients, uniform inflow; (**b**) lift coefficients, T.I. of 6.35%; (**c**) lift coefficients, T.I. of 10.18%; (**d**) pressure drag coefficients, uniform inflow; (**e**) pressure drag coefficients, T.I. of 6.35%; (**f**) pressure drag coefficients, T.I. of 10.18%.

3.4. Pitching Moment Damping Analysis

A sharp change in the pitching moment would cause flutter. Therefore, it was necessary to conduct relevant research on C_m under turbulent conditions. Figure 10 illustrates the comparison of C_m of the deep stall case above in a pitching cycle. The small figure in the lower right indicates the AOA for the corresponding time of the cycle. The comparison demonstrates that the C_m got similar trends in a pitch cycle. All curves were in a U shape. When period <20%, that was before the LEV formed, the values of C_m were relatively flat, but the values of the flapped airfoil were more prominent than the baseline airfoil. When the period was >20%, the values dropped sharply. This rapid change in C_m was caused by the vortex structure evolution. When the flow was reattached, that was after the period >60%, and the C_m shifted rapidly in the positive direction. The Gurney flap could increase the lift, but this could be accompanied by a broader range and a higher negative value of C_m. Besides, compared with uniform flow conditions, the increase of T.I. made both the baseline airfoil and flapped airfoil a slight increase in the negative peaks of the C_m. However, the width of negative peaks would be smaller than that of uniform flow conditions.

In addition, in order to quantify the stability of the airfoil state, the aerodynamic damping characteristics were analyzed by evaluating cyclic integral aerodynamic pitching-moment values based on the negative values of damping factor ζ [39].
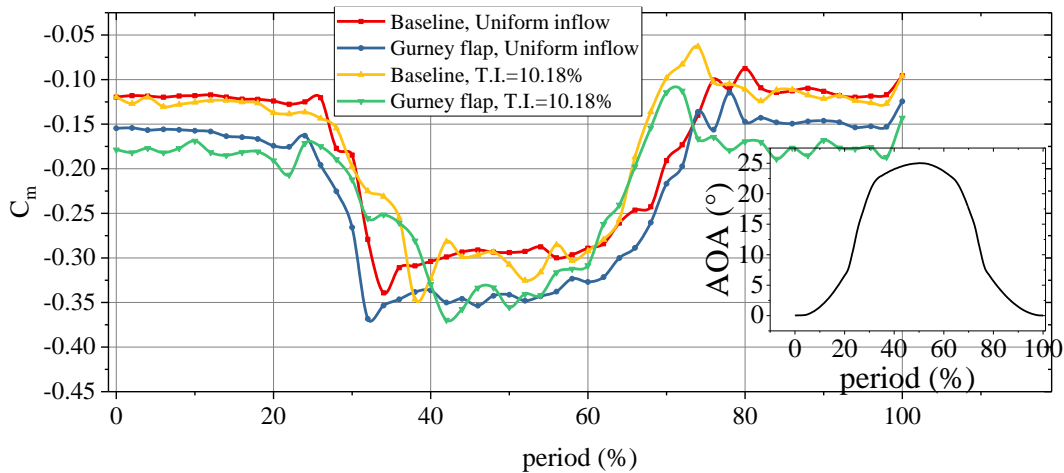
$$\zeta = -\frac{\oint C_m d\alpha}{\pi A^2}.$$ (8)

Figure 10. Comparison of the C_m in a pitching cycle (A = 12.5, α_{mean} = 12.5 and K = 0.0167).

Figure 11 compares the aerodynamic damping coefficients under three different turbulence intensities. In all cases, ζ tended to shift more to the positive direction with the increase of turbulence, which appeared to be in a small direct proportion. The possible reason may be on account of the increase of T.I., the corresponding stall AOA also increased accordingly, making the oscillating airfoil stay in a steady state for a longer time in a cycle. From the results in Figure 11, the addition of a Gurney flap on the trailing edge made the DTU-LN221 airfoil susceptible to stall flutter at uniform flow when A = 10. This situation was considered to be a decrease in the deep stall angle caused by the installation of the flap, leading to an abrupt aerodynamic change. However, in turbulent conditions, the values of ζ deviated in a positive direction after the flap was installed in each case, which has a beneficial effect on the aerodynamic damping. When T.I. = 6.35%, the damping factor ζ increased by 33.33% (when A = 10) and 58.33% (when A = 12.5), respectively, compared with the baseline airfoil condition. In the T.I. = 10.18% condition, the corresponding values were 32.20% (when A = 10) and 34.13% (when A = 12.5), respectively. The flapped airfoil was more stable and tended to be damped.
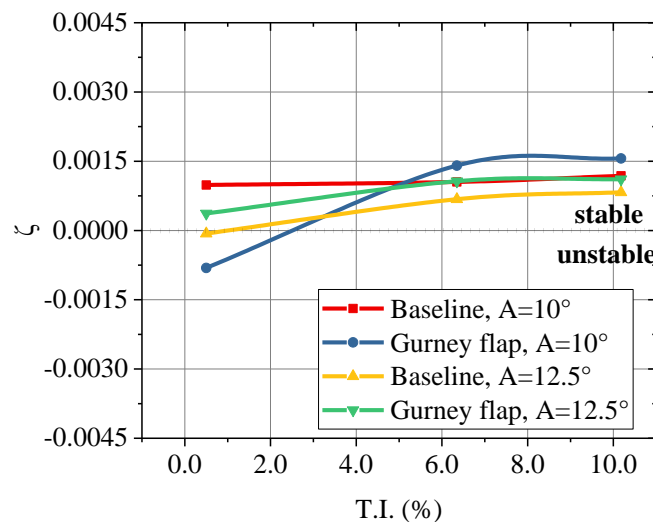

Figure 11. Damping factor at different turbulent inflow.

3.5. Wake Profile Characteristics

For better analysis, in this section, the wake hysteresis of the flow before and after the dynamic stall was investigated to shed light on possible dynamic behavior over the airfoil. Figure 12 shows the wake hysteresis loops for 8.8° to 15.2° pitching motions at

uniform inflow ($A = 3.2$, $\alpha_{\text{mean}} = 12$ and $K = 0.024$, along-wind). The hot wire measuring points were located 0.3 times the chord length downstream of the airfoil. Y was defined as the distance from the trailing edge to the measuring point in the vertical direction (see Figure 2 for details). The suction side was identified as the positive direction, and all the wake hysteresis loops were generated after averaging the data of multiple cycles. Note that all the curves were phase averaged over multiple oscillation periods. Obviously, due to the asymmetry of the DTU-LN221 airfoil, the wake velocity was also asymmetrical in the relative vertical position. Depending on the wake hysteresis loops, when the vortex at the trailing edge migrated to the airfoil and shed into the wake, varying degrees of the velocity deficit in each position existed.
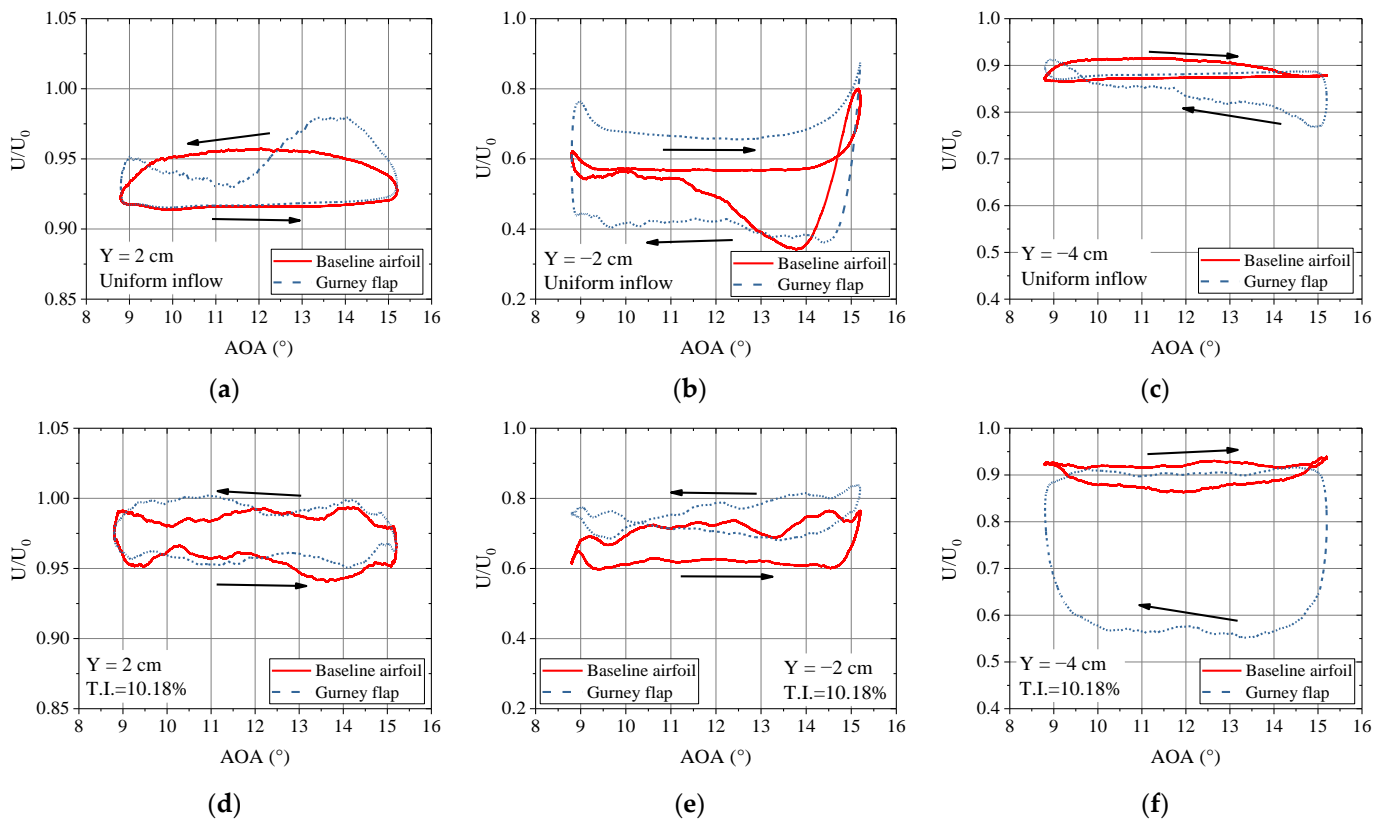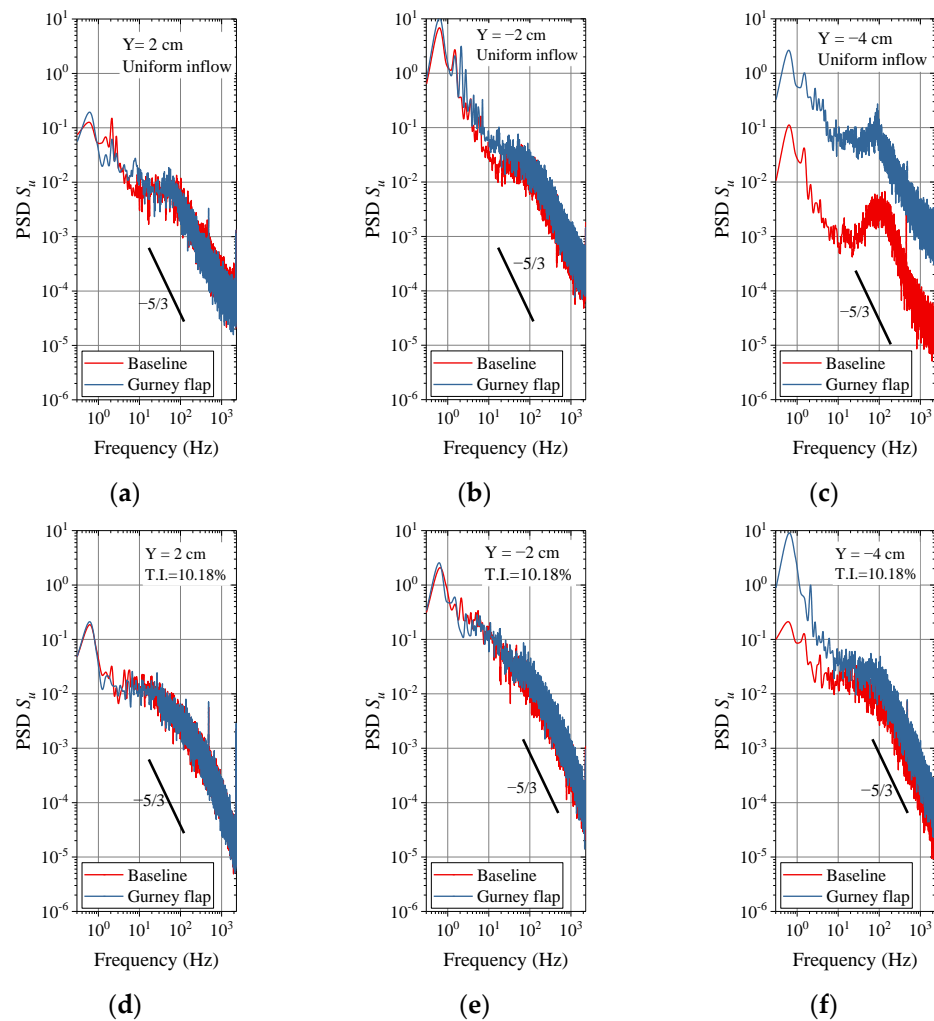

Figure 12. Comparison of wake velocity hysteresis loops. (**a**) uniform inflow, Y = 2 cm; (**b**) uniform inflow, Y = −2 cm; (**c**) uniform inflow, Y = −4 cm; (**d**) T.I. = 10.18%, Y = 2 cm; (**e**) T.I. = 10.18%, Y = −2 cm; (**f**) T.I. = 10.18%, Y = −4 cm.

In the uniform inflow cases, the wake hysteresis loops changed counterclockwise along with the AOA in the positions of the suction side. While on the pressure side, the wake hysteresis loops changed clockwise along with the AOA. Look into the suction surface, at the position of Y = 2 cm (see Figure 12a), the flapped airfoil performed a similar wake hysteresis loop with the baseline airfoil, and both the baseline airfoil and flapped airfoil got the greatest velocity deficit at the position of Y = −2 cm (see Figure 12b). In this figure significant differences between the widths of two loops were observed, the flapped airfoil had a larger velocity deficit and a wider hysteresis loop. For example, at AOA ≈ 12.0°, the width of the hysteresis loop for flapped airfoil was about 3.1 times more than that of baseline airfoil.

In the turbulent inflow cases, the velocity deficit of the baseline airfoil was more apparent from Y = 2 cm to Y = −2 cm (see Figure 12d,e), the hysteresis loops kept the same counterclockwise direction. In contrast, the flapped airfoil got the greatest at the position of Y = −4 cm (see Figure 12f), the velocity deficit of the flapped airfoil was more deflected to the pressure side. The increase of T.I. and installation of a Gurney flap reduced

the size of the wake affected area on the suction surface and expanded the area on the pressure surface.

In Figure 13, the frequency domain comparisons of the PSD along-wind were reported for wake hysteresis loops. In all cases, the highest peaks at low frequencies (≈0.76 Hz) indicated the periodic characteristics of the pitching airfoil. In the uniform inflow, the fluctuations near low frequencies (1 to 10 Hz) were believed to be caused by the boundary layer development, such as the transition and separation of vortices and the pitch motion coupled by the airfoil in the flow field. The peaks at approximately 90 to 100 Hz demonstrated the dominant frequency of the vortices in the wake, and the peaks were more pronounced on the pressure side. In the position of Y = −4 cm, the apparent fluctuation was found in a higher frequency position, implying that the vortices were broken into smaller scales in this position. Comparing the spectrum in all uniform cases, baseline airfoil and flapped airfoil values were relatively similar on the suction side. While on the pressure side, the flapped airfoil appeared more energy through higher amplitudes. It should be noted that compared to the static cases in the previous study, the fluctuations caused by the Gurney flap were not found in dynamic conditions. The vortices caused by the Gurney flap were affected by the coupling of the periodic oscillation and the dynamic vortices of the various scales. Hence, the corresponding fluctuation was not significant in the frequency domain.

Figure 13. Comparison of the along wind PSD of the wake hysteresis loops. (**a**) uniform inflow, Y = 2 cm; (**b**) uniform inflow, Y = −2 cm; (**c**) uniform inflow, Y = −4 cm; (**d**) T.I. = 10.18%, Y = 2 cm; (**e**) T.I. = 10.18%, Y = −2 cm; (**f**) T.I. = 10.18%, Y = −4 cm.

While in the turbulent inflow, due to the disarray of incoming flow, the wake vortices appeared only at the position Y = −4 cm. It is because after the dynamic stall occurs, the LEV starts to shed and away from the surface. Hence, the peak value representing vortex shedding frequency appeared in the wake. The boundary layer in turbulent inflow can resist higher adverse pressure gradients than uniform inflow conditions, so the separated shear layer was not easy to be rolled up. Correspondingly, the peak value in turbulent flow conditions was not apparent. Meanwhile, we observed the same trend from the across-wind. Besides, due to the wake deflection, the difference between the baseline airfoil and the flapped airfoil was mainly on the pressure side. The power spectrum amplitudes of the suction side were smaller than the pressure side. Note that turbulence made the difference between baseline airfoil and flapped airfoil smaller.

4. Conclusions

In this paper, the aerodynamic characteristics of the Gurney flap on a pitching DTU-LN221 airfoil were investigated at Re = 1.5×10^5, and a brief comparison of aerodynamic damping factors between the baseline airfoil and flapped airfoil was presented. This work is different from our previous studies about the aerodynamic changes of a static airfoil [38]. According to the experiment results, the conclusions can be drawn as follows:

As a flow control device on the pressure surface of the trailing edge, the present light stall and deep stall measurements indicated that the influence of a Gurney flap on dynamic aerodynamic performance was significant. Compared with the uniform inflow, the Gurney flap leads to an additional increase in lift and pitching moment under turbulent conditions. Although the increasing amplitude of the maximum lift decreased with a higher T.I., the lift hysteresis loop showed that the Gurney flap could improve lift at most of the period under turbulent conditions. The flapped airfoil made the velocity deficit on the pressure surface more remarkable by measuring the near wake flow than the baseline airfoil. With the increase of T.I., the wake deflected more to the pressure side, and the wake vortices were not apparent in the pitching motion of the airfoil. From a simple aerodynamic damping analysis, the flapped airfoil was more stable in turbulent conditions, although it markedly increased the pitching-moment peak. By comparing the aerodynamic performance of airfoil with Gurney flaps in turbulent conditions, it seems that an offshore wind turbine made up of DTU-LN221 airfoils for practical operation, the form of an active Gurney flap seems not a necessary condition for power optimization.

It is worth noting that the natural inflow of the wind turbines is usually the instantaneous variation of gusts combined with the rotating wake of the wind turbine in front. The study of the lift increment of the Gurney flap also needs to be combined with three-dimensional rotation, which constantly interacts with this highly unsteady aerodynamic problem. Therefore, to more accurately analyze the effect of the combination of this turbulence level with the Gurney flap, subsequent research needs to carry out the rotation combined with shear inflow. This experiment is currently being done on a small scale wind turbine consisting of the DTU-LN221 airfoil sections.

Author Contributions: Conceptualization, H.Y.; conducted the data collection, J.Y.; funding acquisition, H.Y.; supervision, N.L. and H.Y.; writing—original draft preparation, J.Y.; writing—review and editing, H.Y. and X.W. All authors have read and agreed to the published version of the manuscript.

Institutional Review Board Statement: Not applicable.

Informed Consent Statement: Not applicable.

Data Availability Statement: All data generated or analyzed during this study are included in this manuscript.

Conflicts of Interest: The authors declare no conflict of interest.

References

1. Liebeck, R.H. Design of subsonic airfoils for high lift. *J. Aircr.* **1978**, *15*, 547–561. [CrossRef]
2. Jeffrey, D.; Zhang, X.; Hurst, D.W. Aerodynamics of Gurney flaps on a single-element high-lift wing. *J. Aircr.* **2000**, *37*, 295–301. [CrossRef]
3. Cole, J.A.; Vieira, B.A.O.; Coder, J.G.; Premi, A.; Maughmer, M.D. An Experimental Investigation into the Effect of Gurney Flaps on Various Airfoils. *J. Aircr.* **2013**, *50*, 1287–1294. [CrossRef]
4. Holst, D.; Bach, A.B.; Nayeri, C.N.; Paschereit, C.O.; Pechlivanoglou, G. Wake Analysis of a Finite Width Gurney Flap. *J. Eng. Gas Turb. Power* **2016**, *138*, 062602. [CrossRef]
5. Zhu, H.T.; Hao, W.X.; Li, C.; Ding, Q.W. Numerical study of effect of solidity on vertical axis wind turbine with Gurney flap. *J. Wind. Eng. Ind. Aerod.* **2019**, *186*, 17–31. [CrossRef]
6. Wang, J.J.; Li, Y.C.; Choi, K.S. Gurney flap—lift enhancement, mechanisms and applications. *Prog. Aerosp. Sci.* **2008**, *44*, 22–47. [CrossRef]
7. Zhang, Y.; Ramdoss, V.; Saleem, Z.; Wang, X.F.; Schepers, G.; Ferreira, C. Effects of root Gurney flaps on the aerodynamic performance of a horizontal axis wind turbine. *Energy* **2019**, *187*, 115955. [CrossRef]
8. Kentfield, J.A.C. Theoretically and experimentally obtained performances of gurney-flap equipped wind turbines. *Wind Eng.* **1994**, *18*, 63–74.
9. Kentfield, J.A.C. The influence of free-stream turbulence intensity on the performance of Gurney-flap equipped wind-turbine blades. *Wind Eng.* **1996**, *20*, 93–106.
10. Bak, C.; Zahle, F.; Bitsche, R.; Kim, T.; Yde, A.; Henriksen, L.C.; Natarajan, A.; Hansen, M.H. *Description of the DTU 10 MW Reference Wind Turbine*; DTU Wind Energy Report-I-0092; Technical University of Denmark: Roskilde, Denmark, 2013.
11. Ebrahimi, A.; Movahhedi, M. Wind turbine power improvement utilizing passive flow control with microtab. *Energy* **2018**, *150*, 575–582. [CrossRef]
12. Yan, Y.; Avital, E.J.; Williams, J.; Cui, J.H. Performance Improvements for a Vertical Axis Wind Turbine by Means of Gurney Flap. *J. Fluids Eng.* **2019**, *142*, 021205. [CrossRef]
13. Alber, J.; Soto-Valle, R.; Manolesos, M.; Bartholomay, S.; Nayeri, C.N.; Schöenlau, M.; Menzel, C.; Paschereit, C.O.; Twele, J.; Fortmann, J. Aerodynamic effects of Gurney flaps on the rotor blades of a research wind turbine. *Wind Energy Sci.* **2020**, *5*, 1645–1662. [CrossRef]
14. Vestas. Improving turbine performance with Vortex Generators and Gurney Flaps. Available online: http://nozebra.ipapercms.dk/Vestas/Communication/Productbrochure/ProductImprovements/AerodynamicUpgrades/?pag=1 (accessed on 4 March 2022).
15. McCroskey, W. Unsteady Airfoils. *Annu. Rev. Fluid Mech.* **1982**, *14*, 285–311. [CrossRef]
16. Leishman, J.G. Challenges in modelling the unsteady aerodynamics of wind turbines. *Wind Energy* **2002**, *5*, 85–132. [CrossRef]
17. Gharali, K.; Johnson, D.A. Dynamic stall simulation of a pitching airfoil under unsteady freestream velocity. *J. Fluid Struct.* **2013**, *42*, 228–244. [CrossRef]
18. Mulleners, K.; Raffel, M. Dynamic Stall Development. *Exp. Fluids* **2013**, *54*, 1469. [CrossRef]
19. Gupta, R.; Ansell, P.J. Unsteady Flow Physics of Airfoil Dynamic Stall. *AIAA J.* **2019**, *57*, 165–175. [CrossRef]
20. Rival, D.; Tropea, C. Characteristics of pitching and plunging airfoils under dynamic-stall conditions. *J. Aircr.* **2010**, *47*, 80–86. [CrossRef]
21. Masdari, M.; Seyednia, M.; Tabrizian, A. An experimental loading study of a pitching wind turbine airfoil in near-and post-stall regions. *J. Mech. Sci. Technol.* **2018**, *32*, 3699–3706. [CrossRef]
22. Tabrizian, A.; Masdari, M.; Tahani, M. Surface Pressure Study of an Airfoil Undergoing Combined Pitch and Low-Amplitude Plunge Motions. *J. Appl. Fluid Mech.* **2019**, *12*, 1957–1966. [CrossRef]
23. Mamouri, A.R.; Khoshnevis, A.B.; Lakzian, E. Experimental study of the effective parameters on the offshore wind turbine's airfoil in pitching case. *Ocean Eng.* **2020**, *198*, 106955. [CrossRef]
24. Gerontakos, P.; Lee, T. Oscillating Wing Loadings with Trailing-Edge Strips. *J. Aircr.* **2006**, *43*, 428–436. [CrossRef]
25. Masdari, M.; Mousavi, M.; Tahani, M. Dynamic stall of an airfoil with different mounting angle of Gurney flap. *Aircr. Eng. Aerosp. Technol.* **2020**, *92*, 1037–1048. [CrossRef]
26. Zanotti, A.; Gibertini, G. Experimental assessment of an active L-shaped tab for dynamic stall control. *J. Fluids Struct.* **2018**, *77*, 151–169. [CrossRef]
27. Li, Q.; Kamada, Y.; Maeda, T.; Murataet, J.; Nishida, Y. Effect of turbulent inflows on airfoil performance for a Horizontal Axis Wind Turbine at low Reynolds numbers (Part II: Dynamic pressure measurement). *Energy* **2016**, *112*, 574–587. [CrossRef]
28. Cheng, J.T.; Zhu, W.J.; Fischer, A.; García, N.R.; Madsen, J.; Chen, J.; Shen, W.Z. Design and validation of the high performance and low noise CQU-DTU-LN1 airfoils. *Wind Energy* **2013**, *17*, 1817–1833. [CrossRef]
29. ROHA. *LSWT Campaign Report on DTU-C21*; LM Internal Report; ROHA: Jupitervej, Denmark, 2012.
30. Vita, G.; Hemida, H.; Andrianne, T.; Baniotopoulos, C.C. Generating atmospheric turbulence using passive grids in an expansion test section of a wind tunnel. *J. Wind. Eng. Ind. Aerod.* **2018**, *178*, 91–104. [CrossRef]
31. Choudhry, A.; Leknys, R.; Arjomandi, M.; Kelso, R. An insight into the dynamic stall lift characteristics. *Exp. Therm. Fluid Sci.* **2014**, *58*, 188–208. [CrossRef]

32. Granlund, K.; Ol, M.; Garmann, D.; Visbal, M. Experiments and Computations on Abstractions of Perching. In Proceedings of the 28th AIAA Applied Aerodynamics Conference, Chicago, IL, USA, 28 June–1 July 2010.

33. Li, S.; Zhang, L.; Xu, J.; Yang, K.; Guo, G. Experimental investigation of a pitch-oscillating wind turbine airfoil with vortex generators. *J. Renew. Sustain. Energy* **2020**, *12*, 063304. [CrossRef]

34. Masdari, M.; Ghorbani, M.; Tabrizian, A. Experimental study of wake steadiness of an airfoil in pitch–hold–return motion. *Aircr. Eng. Aerosp. Technol.* **2020**, *92*, 1019–1025. [CrossRef]

35. Gardner, A.D.; Wolf, C.C.; Raffel, M. Review of measurement techniques for unsteady helicopter rotor flows. *Prog. Aerosp. Sci.* **2019**, *111*, 100566. [CrossRef]

36. Tavernier, D.D.; Ferreira, C.; Viré, A.; LeBlanc, B.; Bernardy, S. Controlling dynamic stall using vortex generators on a wind turbine airfoil. *Renew. Energy* **2021**, *172*, 1194–1211. [CrossRef]

37. Vita, G.; Hemida, H.; Andrianne, T.; Baniotopoulos, C. The effect of the integral length scale of turbulence on a wind turbine aerofoil. *J. Wind. Eng. Ind. Aerod.* **2020**, *204*, 104235. [CrossRef]

38. Yang, J.W.; Yang, H.; Zhu, W.J.; Li, N.L.; Yuan, Y.P. Experimental study on aerodynamic characteristics of a Gurney flap on a wind turbine airfoil under high turbulent flow condition. *Appl. Sci.* **2020**, *10*, 7258. [CrossRef]

39. Carta, F.O. An Analysis of the Stall Flutter Instability of Helicopter Rotor Blades. *J. Am. Helicopter Soc.* **1967**, *12*, 1–8. [CrossRef]